Turbulent Heating between 0.2 and 1 au: A Numerical Study

Victor Montagud-Camps[1] , Roland Grappin[1] , and Andrea Verdini[1,2]

[1] LPP, Ecole Polytechnique, CNRS, UPMC Univ Paris 06, Univ. Paris-Sud, Observatoire de Paris, Université Paris-Saclay, Sorbonne Universités, PSL Research University, 91128 Palaiseau, France; Victor.Montagud-camps@lpp.polytechnique.fr, Roland.Grappin@lpp.polytechnique.fr

[2] Università di Firenze, Dipartimento di Fisica e Astronomia, Italy; Verdini@arcetri.astro.it

Abstract

The heating of the solar wind is key to understanding its dynamics and acceleration process. The observed radial decrease of the proton temperature in the solar wind is slow compared to the adiabatic prediction, and it is thought to be caused by turbulent dissipation. To generate the observed $1/R$ decrease, the dissipation rate has to reach a specific level that varies in turn with temperature, wind speed, and heliocentric distance. We want to prove that MHD turbulent simulations can lead to the $1/R$ profile. We consider here the slow solar wind, characterized by a quasi-2D spectral anisotropy. We use the expanding box model equations, which incorporate into 3D MHD equations the expansion due to the mean radial wind, allowing us to follow the plasma evolution between 0.2 and 1 au. We vary the initial parameters: Mach number, expansion parameter, plasma β, and properties of the energy spectrum as the spectral range and slope. Assuming turbulence starts at 0.2 au with a Mach number equal to unity, with a 3D spectrum mainly perpendicular to the mean field, we find radial temperature profiles close to $1/R$ on average. This is done at the price of limiting the initial spectral extent, corresponding to the small number of modes in the inertial range available, due to the modest Reynolds number reachable with high Mach numbers.

Key words: magnetohydrodynamics (MHD) – methods: numerical – solar wind – Sun: heliosphere – turbulence

1. Introduction

The radial evolution of the proton temperature in the solar wind has not yet been fully explained. From 0.2 to 1 au, the wind expands radially and with a low-varying mean velocity. Observations have shown that the rate at which the proton temperature decreases in this interval does not correspond to an adiabatic cooling of a spherically expanding flow; instead of a temperature evolution given by $T \propto R^{-4/3}$, a slower cooling rate is observed, $T \propto R^{-\xi}$ for $\xi \in [0.8, 1]$ (Totten et al. 1995). The origin of this extra heating may be attributed to the development of a turbulent regime in the wind that generates substantial heating (e.g., Vasquez et al. 2007; Carbone et al. 2009; Matthaeus & Velli 2011; Coburn et al. 2012; but see also Hellinger et al. 2013 and Scudder 2015 for an explanation not based on the turbulent cascade origin).

We know that in quasi-stationary incompressible turbulence, the turbulent energy (i.e., the sum of the kinetic and magnetic energies) cascades along the inertial range without being dissipated. When energy reaches the dissipation scales, it is transformed into heat. If the process is quasi-stationary, the heating rate can be obtained either from the dissipation rate (if the small-scale dissipation process is known) or via the energy cascade rate. The dissipation mechanisms take place at sub-ion scales that are not yet reachable by current measurements; therefore, little can be said about the associated heating. On the contrary, the cascade rate can be computed at much larger (inertial range) scales, and this is the approach commonly used in analyzing solar wind data to obtain the turbulent heating.

To understand if turbulent heating is responsible for the nonadiabatic decrease of temperature in the solar wind, one needs to compute the heating rate required to produce the observed temperature profile. Such heating is obtained by exploiting an argument based on the internal energy equation (e.g., Vasquez et al. 2007; see Section 2.3 below). In particular, it shows that the existence of a radial power law implies a direct relation between the energy cascade rate Q, wind velocity U,

proton temperature T_p, and heliocentric distance R,

$$Q = (1/2)(k_B/m)UT_p/R, \qquad (1)$$

the coefficient $1/2$ being associated with the scaling $T_p \propto 1/R$, which we adopt here as a representative scaling. Equation (1) expresses a balance between two decaying quantities: the energy cascade rate, which is a turbulent quantity, and the proton temperature, which is not.

The most accurate measurements of the cascade rate are obtained by computing third-order moments of the distribution of the magnetic field (Politano & Pouquet 1998). Such measurements have shown that Equation (1) holds at 1 au (Stawarz et al. 2009; Coburn et al. 2012) and at larger distances (Marino et al. 2008), although the precise value of the cascade rate somewhat depends on the hypothesis made on the 3D geometry of the angular spectra (Verdini et al. 2015).

The existence of the $1/R$ profile between 0.3 and 1 au suggests that the balance in Equation (1) is also realized during this whole distance range, but there is presently no measure of the cascade rate and no proof (either theoretical or numerical) that such an equilibrium is indeed achieved in the inner heliosphere. In fact, previous attempts to verify Equation (1) used models of solar wind turbulence with simplified nonlinear couplings (Tu 1988; Tu & Marsch 1997; Smith et al. 2001; Breech et al. 2009). These models actually managed to reproduce the wind temperature decrease; however, they relied on the choice of free parameters to fit their results to the observations.

We aim here to examine at what conditions such a relation between turbulent heating and temperature, as well as the associated temperature profile, can be found using direct numerical simulations. It is indeed most probable that not all turbulent conditions close to the Sun are able to generate such a close adjustment between the turbulent cascade rate and the temperature in the distance range 0.3–1 au, so that the numerical solution to this problem will provide constraints on turbulent properties close to the Sun.

Figure 1. Initial and final domains of simulation (and plasma volume) in the ecliptic plane. Thin lines: direction of mean magnetic field. For all runs, the aspect ratio of the domain varies from 1/5 to unity. In the figure, the mean magnetic field angle with the radial varies varies from $\tan^{-1}(1/5) \simeq 11°3$ to $\tan^{-1}(1) = \pi/4$.

We directly compute the temperature and heating evolution versus distance, adopting successively different initial states of the plasma at the minimum heliocentric distance (here 0.2 au). We use the MHD equations modified by expansion, as given by the expanding box model (EBM; Grappin et al. 1993). We study in this work the case of the slow solar wind, where turbulence is mainly in a 2D geometry (Dasso et al. 2005; Verdini & Grappin 2016). The initial conditions found to lead to Equation (1) between 0.2 and 1 au will be characterized by (i) spectral properties and (ii) global plasma properties such as expansion parameter, Mach number, plasma β, and mean magnetic field angle with radial.

2. Equations, Control Parameters, Diagnostic Tools, and Initial Conditions

2.1. EBM Equations (Ideal)

We give here a short description of the EBM equations (Grappin et al. 1993; Grappin & Velli 1996; Dong et al. 2014) that allow us to follow the turbulent evolution transported by the radial wind. Let us denote by $\boldsymbol{U}_0 = U_0 \hat{\boldsymbol{e}}_r$ the mean wind velocity.

The wind is assumed to be radial and have a uniform speed ($U_0 = $ const). The radius R at which the numerical domain is located varies with time τ as

$$R(\tau) = R_0 + U_0\tau, \qquad (2)$$

where R_0 is the initial position of the box. Space, time, velocity, temperature, and density are measured in the following units:

$$L_0/(2\pi), \qquad (3)$$

$$t_{\mathrm{NL}}^0 = L_0/(2\pi u_{\mathrm{rms}}^0), \qquad (4)$$

$$u_{\mathrm{rms}}^0, \qquad (5)$$

$$m_p(u_{\mathrm{rms}}^0)^2/(2k_B), \qquad (6)$$

and

$$\rho^0, \qquad (7)$$

where ρ^0 is the initial average density of the plasma, u_{rms}^0 is the initial rms velocity of the fluctuations, t_{NL}^0 is the initial nonlinear time based on the initial rms velocity, and L_0 is the initial size of the numerical domain perpendicular to the radial direction.

The EBM approach relies on the idea that a simple change of Galilean frame is not sufficient to eliminate the expansion. After such a frame change, the plasma still expands: it is stretched in directions perpendicular to the radial. In other words, a systematic velocity field perpendicular to the mean radial direction remains. To recover the usual theoretical setup where the fluctuating quantities are homogeneous (i.e., have zero average) in the plasma volume, we need to subtract this

transverse expansion. This is done by using coordinates comobile with this transverse expansion:

$$t = \tau, \qquad (8)$$

$$x = (X - U_0\tau)/a_x, \qquad (9)$$

$$y = Y/a(t), \qquad (10)$$

and

$$z = Z/a(t). \qquad (11)$$

The parameter $a_x = L_x/L_y = L_x/L_z = 5$ is the initial aspect ratio of the domain. The parameter a is defined as the normalized heliospheric distance,

$$a = R(t)/R_0 = 1 + \epsilon t, \qquad (12)$$

where $\epsilon = da/dt$ is the expansion parameter defined as the initial ratio between the characteristic expansion and turnover times in the transverse directions (perpendicular to the radial),

$$\epsilon = \frac{\tau_{\mathrm{NL}}}{\tau_{\mathrm{exp}}} = \frac{U_0/R_0}{k_0 u_{\mathrm{rms}}}, \qquad (13)$$

with k_0 the minimum wavenumber in the transverse direction. At a given distance $R(t)$, the domain thus has an aspect ratio $L_\perp/L_{\mathrm{radial}} = a(t)/a_x$.

The EBM equations with dissipation terms omitted (but see Equations (20) and (21) below) read

$$\partial_t\rho + \nabla(\rho\boldsymbol{u}) = -2\rho(\epsilon/a), \qquad (14)$$

$$\partial_t P + (\boldsymbol{u}.\nabla)P + \gamma P\nabla.\boldsymbol{u} = -2\gamma P(\epsilon/a), \qquad (15)$$

$$\partial_t\boldsymbol{u} + \boldsymbol{u}.\nabla\boldsymbol{u} + \nabla(P + B^2/2)/\rho - \boldsymbol{B}.\nabla\boldsymbol{B}/\rho = -\vec{\mathbb{U}}(\epsilon/a), \qquad (16)$$

$$\partial_t\boldsymbol{B} + \boldsymbol{u}.\nabla\boldsymbol{B} - \boldsymbol{B}.\nabla\boldsymbol{u} + \boldsymbol{B}\nabla.\boldsymbol{u} = -\vec{\mathbb{B}}(\epsilon/a), \qquad (17)$$

and

$$P = \rho T. \qquad (18)$$

In these equations, ρ is the density, P is the total pressure, B is the magnetic field, and u is the velocity fluctuation $u = U - U_0\hat{e}_r$, U being the total velocity. The pressure equation with $\gamma = 5/3$ is the perfect gas equation, and $T = T_i = T_e$ is the proton (and electron) temperature, m_p being the proton mass.

The above equations are standard MHD equations with, however, two modifications. First, additional linear terms involving the constant average speed U_0 appear on the right-hand side: $\mathbb{U} = (0, u_y, u_z)$ and $\mathbb{B} = (2B_x, B_y, B_z)$. Hence, depending on the component, the right-hand side damping term differs, as is well known. Note that in the following, we will sometimes use the dimensional form of these damping terms, namely, with $\epsilon/a(t) \rightarrow U_0/R(t)$. Second, a new expression for the gradients is used, accounting for the increasing lateral stretching of the plasma volume with time/distance:

$$\nabla = ((1/a_x)\partial_x, (1/a(t))\partial_y, (1/a(t))\partial_z), \qquad (19)$$

With Ox being along the radial, expansion acts only in the other two directions.

All fields $\rho(x, y, z), u(x, y, z)$, etc. are then considered to be periodic in all three directions of the domain comobile with the mean expansion. This allows to use a pseudo-spectral method

for the spatial scheme, as in the standard Lagrangian approach. The temporal scheme is a third-order Runge–Kutta method.

2.2. Defining Visco-resistive Terms and Dissipation Rate

The diffusive terms read

$$\partial_t \boldsymbol{u}|_{\text{dis}} = (\mu/\tilde{\rho})(\tilde{\nabla}^2 \boldsymbol{u} + (1/3)\tilde{\nabla}(\tilde{\nabla} \cdot \boldsymbol{u})), \tag{20}$$

$$\partial_t \boldsymbol{B}|_{\text{dis}} = \eta \tilde{\nabla}^2 \boldsymbol{B}, \tag{21}$$

and

$$\partial_t P|_{\text{dis}} = \bar{\rho}\kappa \tilde{\Delta} T, \tag{22}$$

where $\tilde{\rho}$ is the density normalized by its average,

$$\tilde{\rho} = \rho/\bar{\rho} = a^2 \rho, \tag{23}$$

and $\bar{\rho} = 1/a^2$ is the average density of the plasma. Note that the normalized density $\tilde{\rho}$ is unity, on average. Note that density enters in two different ways in the dissipative terms: as the normalized density $\tilde{\rho}$ in the momentum equation and as the average $\bar{\rho}$ in the pressure equation. In the homogeneous (nonexpanding) case, the dissipative terms given by Equations (20) and (21) are identical to the standard ones in MHD. In the expanding case, these dissipation terms have two specific differences. First, the ∇ operator components are comobile derivatives, without the anisotropic prefactors $(1/a_x, 1/a, 1/a)$:

$$\tilde{\nabla} = (\partial_x, \partial_y, \partial_z). \tag{24}$$

This allows the dissipation to be isotropic in comobile coordinates, that is, to use the available Fourier domain most efficiently. Second, we impose that viscosity, resistivity, and conductivity κ decrease as time/distance increases (see Equation (12)):

$$\kappa = \mu = \eta = \mu_0/a. \tag{25}$$

This choice allows us to somewhat moderate the decrease of the Reynolds number associated with the fast damping of the turbulent amplitude.

From Equations (20) and (21), one derives the contribution of dissipative terms to the turbulent energy evolution,

$$\frac{d}{dt}(\rho u^2/2 + B^2/2)|_{\text{diss}} = -\bar{\rho}Q_\nu + \tilde{\nabla} \cdot F, \tag{26}$$

where F is a flux that does not change the average turbulent energy. The turbulent heating is given by the visco-resistive damping term Q_ν, which is always positive,

$$Q_\nu = \mu(\tilde{\omega}^2 + 4/3(\tilde{\nabla} \cdot u)^2) + \eta \tilde{J}^2, \tag{27}$$

where $\tilde{\omega} = \tilde{\nabla} \times u$ and $\tilde{J} = \tilde{\nabla} \times B$.

Finally, what is lost by turbulent energy is transmitted to internal energy; this reads

$$\partial_t P + (\boldsymbol{u}.\nabla)P + \gamma P\nabla.\boldsymbol{u}$$
$$+ 2\gamma P(\epsilon/a) = \bar{\rho}\kappa \tilde{\Delta} T + (\gamma - 1)\bar{\rho}Q_\nu, \tag{28}$$

where κ is the thermal conductivity. Since we are in the following more directly interested in the temperature T, we also write down its equation:

$$\partial_t T + (\boldsymbol{u}.\nabla)T + (\gamma - 1)T\nabla.\boldsymbol{u} + 2(\gamma - 1)T(\epsilon/a)$$
$$= (\kappa/\tilde{\rho})\tilde{\Delta} T + (\gamma - 1)Q_\nu/\tilde{\rho}. \tag{29}$$

2.3. Critical Heating, Cascade Rate, and Parameter M^2/ϵ

We here rederive Equation (1), which expresses the critical heating leading to a temperature decrease as $T_p \propto 1/R$. For this, we need to take the spatial average of Equation (29), so eliminating the thermal conductive term. The other terms are checked to be negligible, e.g., using the dimensional factor U_0/R instead of $\epsilon/a(t)$,

$$\overline{\boldsymbol{u}.\nabla T} = \overline{\boldsymbol{u}.\nabla \delta T} \ll 2\gamma \bar{T} U_0/R, \tag{30}$$

which gives for the average temperature (the spatial average being denoted either by a bar or by angular brackets)

$$\partial_t \bar{T} + 2(\gamma - 1)\bar{T}(\epsilon/a) = (\gamma - 1)\langle Q_\nu/\tilde{\rho}\rangle \simeq (\gamma - 1)\overline{Q_\nu}, \tag{31}$$

where the last equality is obtained assuming $\delta\rho/\rho \ll 1$. Now we replace the temporal derivative by the radial derivative, $\partial_l \to U_0 \partial_R$, and the damping term ϵ/a by its dimensional expression $U_0/R(t)$,

$$U_0 \partial_R \bar{T} + 2(\gamma - 1)\bar{T}(U_0/R) \simeq (\gamma - 1)\overline{Q_\nu}. \tag{32}$$

We now define Q_α as the heating necessary to obtain a temperature profile of the form $T = 1/R^\alpha$. Thus, we replace in Equation (32) $U_0 d\bar{T}/dR = -\alpha U_0 \bar{T}/R$; this gives

$$Q_\alpha = \frac{4 - 3\alpha}{2}\bar{T}U_0\big/R. \tag{33}$$

In the following, we will insist on the special value $\alpha = 1$, which leads to what we will call the critical heating Q_c:

$$Q_c = Q_1 = (1/2)\bar{T}U_0/R. \tag{34}$$

Using simple phenomenology, we now derive a condensed formula for such a critical heating involving basic parameters of the turbulent wind: the Mach number and the expansion parameter ϵ. We first define the Kolmogorov cascade rate, generalized to MHD, in two ways. A first definition (Vasquez et al. 2007) is given by

$$Q_{K41} \simeq k(u^2 + \delta B^2/\rho)^{3/2} \simeq 3ku^3, \tag{35}$$

with $\delta B = B - \langle B\rangle$ being the magnetic field fluctuation and both u and δB being evaluated at the Taylor's scale, thus in the inertial range. In Equation (35), u^2 and $\delta B^2/\rho$ are, respectively, the kinetic and magnetic energy content in the wavenumber range $[k/\sqrt{2}, k\sqrt{2}]$, where k lies in the inertial range. Note that to derive the last approximate equality, we have assumed equipartition between kinetic and magnetic energy.

When analyzing our simulation results, we shall use the equivalent but more precise definition,

$$Q_{K41} = E(k_\lambda)^{3/2}k_\lambda^{5/2}, \tag{36}$$

3

where $E(k_\lambda)$ is twice the 1D total (kinetic+magnetic) energy spectrum, integrated on directions perpendicular to the radial and depending on the radial wavenumber, evaluated at the Taylor's wavenumber k_λ. The Taylor wavenumber is defined as

$$k_\lambda = \frac{\left(\int_0^\infty k_x^2 E(k_x) dk_x\right)^{1/2}}{\int_0^\infty E(k_x) dk_x}. \qquad (37)$$

More precisely, k_λ marks the middle of the inertial zone of the reduced spectrum in the radial direction.

Now, we know from Vasquez et al. (2007) that in cold winds, the Kolmogorov cascade rate Q_{K41} overestimates by a factor of 10 the true average dissipation rate $\overline{Q_\nu}$:

$$Q_{K41} \simeq 10\overline{Q_\nu}. \qquad (38)$$

From the latter equation, Equations (33) and (35), we rewrite the critical condition $Q_\nu = Q_\alpha$ to produce a $1/R^\alpha$ temperature profile as

$$3ku^3 \simeq 10 \, \frac{4-3\alpha}{2} \overline{T} U_0 \Big/ R. \qquad (39)$$

We want to express this condition in terms of the rms turbulent Mach number,

$$M = u_{\rm rms}/c_s, \qquad (40)$$

where $c_s = (\gamma P/\rho)^{1/2}$ is the sound speed and the expansion parameter ϵ (Equation (13)), which also includes the rms velocity in its definition. Assuming that the inertial range begins at the largest scale, we evaluate the kinetic energy content at the largest scale $u_0^2/2$ and the total energy content $u^2/2$ by integrating a Kolmogorov spectrum $\propto k^{-5/3}$ on, respectively, the interval range $[k_0, 2k_0]$ and $[k_0, \infty]$. This leads to a ratio $(u_{\rm rms}/u_0)^3 = 4.4$, which allows us to express Equation (39) in terms of quantities based on rms velocity amplitude, namely the Mach number M and expansion parameter ϵ. One finds

$$M^2/\epsilon \simeq 4.4(4-3\alpha) \qquad (41)$$

and, for the particular value $\alpha = 1$,

$$M^2/\epsilon \simeq 4.4. \qquad (42)$$

Equation (42) will guide us in selecting "critical" couples of initial Mach number and expansion parameter in our simulations.

2.4. Turbulent Energy, Expansion, and Viscous Damping

We define the average turbulent energy per unit mass:

$$e = \frac{1}{2}\langle \tilde{\rho}u^2 + \delta B^2/\bar{\rho} - \rangle. \qquad (43)$$

From Equations (16) and (17), one finds the expression of the energy damping rate due to expansion,

$$Q_{\rm exp} = \frac{1}{2}\langle \tilde{\rho}(u_y^2 + u_z^2) + \delta B_x^2/\bar{\rho}\rangle(2\epsilon/a), \qquad (44)$$

or, in dimensional terms,

$$Q_{\rm exp} = \frac{1}{2}\langle \tilde{\rho}(u_y^2 + u_z^2) + \delta B_x^2/\bar{\rho}\rangle(2U_0/R). \qquad (45)$$

The two main terms leading to the damping of turbulent energy are thus (i) the small-scale diffusive (viscous and resistive) damping term Q_ν, which is fed by the nonlinear turbulent energy cascade, and (ii) the expansion damping term $Q_{\rm exp}$. However, here turbulent energy conservation is subject to further effects: (i) compressibility breaks the turbulent energy invariance, the remaining invariant being the sum of turbulent energy and internal energy; and (ii) expansion modifies the nonlinear terms as well, thus breaking down all inviscid invariants of homogeneous MHD. These two additional effects are gathered in a single term denoted by $Q_{\rm NL}$. It is found by subtracting turbulent dissipation and linear expansion decay from the time derivative of turbulent energy:

$$de/dt = -Q_\nu - Q_{\rm exp} - Q_{\rm NL}. \qquad (46)$$

In the previous equation and from now on, Q_ν (without average) denotes the spatial average $\langle Q_\nu \rangle$. Note that the very existence of a Kolmogorov-like spectral scaling $k^{-5/3}$ implies that the term $Q_{\rm NL}$ should be subdominant compared to Q_ν.

2.5. Numerics, Initial Conditions, and Parameters

All simulations are computed in a numerical box with resolution $N_x = N_y = N_z = 512$. We start at 0.2 au with a numerical box elongated with an aspect ratio $a_x = 5$ along the radial of dimensions $L_x = 5 \times L_y = 5 \times L_z = 5 \times 2\pi$. The domain is then stretched by expansion in directions perpendicular to the radial so that at 1 au the domain becomes a cube, and the mean field rotates accordingly (Figure 1).

We set up energy equipartition: $u_{\rm rms} = b_{\rm rms} = 1$ and about zero correlation between magnetic and velocity fluctuations (zero cross-helicity). Energy isocontours are spatially aniso-tropic, having the same aspect ratio as the numerical box. As the mean magnetic field in all runs makes a small angle θ with the radial (between 11° and 20°), the initial spectrum has isocontours not far from perpendicular to the radial direction with an aspect ratio equal to 5 (see Figure 9(a)). This corresponds to the so-called "2D" configuration characteristic of slow winds (Dasso et al. 2005; Verdini & Grappin 2016).

The parameters of the simulations are listed in Table 1, which lists all runs described here. The main parameters are the Mach number and expansion parameter ϵ. In Table 1, ϵ goes from 0.12 to 0.4, M from 0.3 to 1, and M^2/ϵ from 0.45 to 5. Varying ϵ by a factor of 2 as done here corresponds to varying the initial turnover time of the largest scale by such a factor, so the wavenumber by a factor of $2^{2/3}$, adopting a $k^{-5/3}$ scaling for the initial spectrum. Also, the simulation duration is longer when ϵ is smaller, as the transport distance (from 0.2 to 1 au) is fixed.

Each simulation provides a test window of wavenumbers (reduced to a little more than two decades) on the much larger solar wind inertial range. When choosing the couple (M, ϵ) for a given run, we choose a wind regime, and at the same time we place our simulation range on the solar wind wavenumber range. Typical values, as taken in the runs A, B, C, and E, are $M = 1$ and $\epsilon = 0.2$. Such values are not far from the values

Table 1
List of Parameters for the Initial Conditions

R	M	ϵ	$\frac{M^2}{\epsilon}$	B_0	β	k_{max}	m	μ_0
A	1	0.2	5	2.04	0.29	64	5/3	2.4 10^{-3}
B	1	0.2	5	2.04	0.29	64	3	1.7 10^{-3}
C	1	0.2	5	2.04	0.29	4	5/3	2.1 10^{-3}
D	0.77	0.2	3	2.04	0.49	4	5/3	1.8 10^{-3}
E	1	0.2	5	2.04	0.29	4	2.2	1.7 10^{-3}
F	0.77	0.12	5	2.04	0.49	4	2.2	1.8 10^{-3}
G	0.6	0.14	2.6	2.04	0.8	4	2.2	1.5 10^{-3}
H	1	0.4	2.5	2.04	0.29	4	2.2	1.3 10^{-3}
K	0.77	0.2	3	2.04	0.49	4	2.2	1.8 10^{-3}
M	0.77	0.2	3	0.86	2.75	4	2.2	1.8 10^{-3}
N	0.77	0.2	3	1.17	1.48	4	2.2	1.8 10^{-3}
Z	0.3	0.2	0.45	2.04	0.29	64	5/3	1.5 10^{-4}

Note. In the table, R is the name of the run; $M = u_{rms}/c_s$, with c_s the sound speed; ϵ is the initial expansion parameter; M^2/ϵ, see Section 2.3; B_0 is the initial magnetic field amplitude (and Alfvén speed); β is the ratio of thermal over magnetic pressure; k_{max} is the maximum wavenumber in directions perpendicular to radial (nota bene largest perpendicular scale corresponds to unit wavenumber); m is the 1D spectral slope; and μ_0 is the initial value of the diffusive parameters (viscosity, resistivity, and conduction).

found in cold winds in Helios data at the scale of several hours (Grappin et al. 1991).

As seen in Section 2.3, the expression M^2/ϵ was found to be approximately 4.4 in the inertial range at 1 au by Vasquez et al. (2007) for cold/slow winds. This is in the middle of the range of values listed in Table 1.

Other parameters appearing in Table 1 are the plasma β, $\beta = P_{th}/P_B = (2/\gamma)(c_s/v_a)^2$, which is varied from 0.29 to 1.48, and the mean field B_0, which varies between 0.86 and 2.04, meaning that, since $b_{rms} = 1$, b_{rms}/B_0 varies from 1.2 to 0.5. The initial viscosity μ_0 is about the same in all calculations except for run Z: the origin of this exception will be discussed in Section 4.2. The parameters k_{max} and m are, respectively, the extent of the initial spectrum and its 1D spectral slope.

3. Results

3.1. Run A: Extended Initial Spectrum

We start with the case of run A, with $M = 1$, $\epsilon = 0.2$, and thus $M^2/\epsilon = 5$. The initial spectral extent in the direction perpendicular to the radial is $k_{max} = 64$, and the spectral slope is $m = 5/3$.

Figure 2 shows the evolution of several quantities versus heliocentric distance. Panel (a) shows the evolution of the rms turbulent quantities u_{rms}, $\delta B_{rms}/\bar{\rho}^{1/2}$, and u^c_{rms}, where u^c is the compressible part of the velocity field. The quantities shown are multiplied by $(R/R_0)^{0.6}$. One sees that the compensated profiles of velocity and magnetic field (in velocity units) are close to a plateau, indicating a decay close to $1/R^{0.6}$, somewhat faster than the Wentzel-Kramers-Brillouin (WKB) prediction $u_{rms} \simeq b_{rms}/\bar{\rho}^{1/2} \simeq 1/R^{1/2}$. The compressive rms velocity amplitude, initially zero, rapidly reaches about half that of the total rms velocity and then becomes closer to 1/3 of it. Panel (b) shows the average turbulent dissipation of total (solid line), solenoidal kinetic ($\mu\tilde{\omega}^2$; dotted line), magnetic ($\eta\tilde{J}^2$; dashed line), and compressible ($4/3\mu(\widetilde{\nabla}\cdot u)^2$; dot-dashed line) energy. While the kinetic and magnetic dissipation are
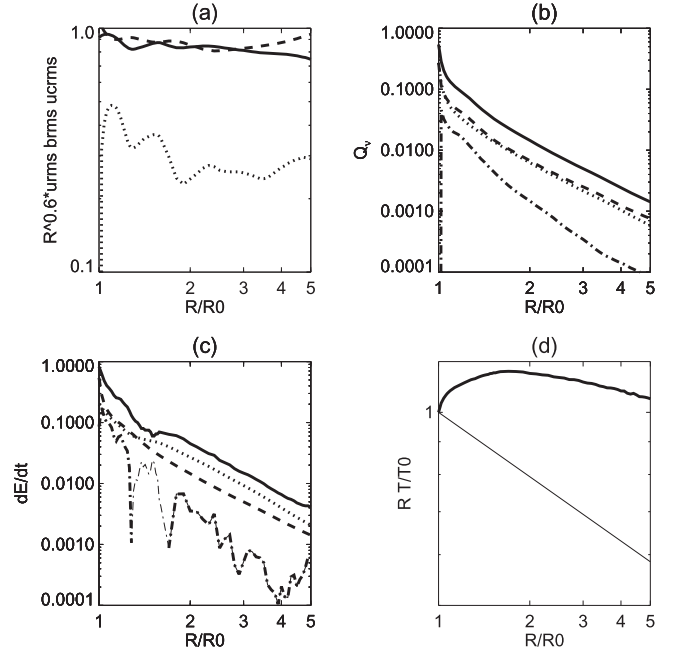
Figure 2. Run A: evolution of basic quantities vs. heliocentric distance R/R_0. (a) Velocity amplitude u_{rms} (solid line), compressible velocity u^c_{rms} (dotted line), and magnetic field fluctuation $b_{rms}/\bar{\rho}^{1/2}$ (dashed line). (b) Visco-resistive dissipation Q_ν (solid line) decomposed as the sum of $\mu|\tilde{\nabla}\times u|^2$ (dotted line), $\eta\tilde{j}^2$ (dashed line), and $\frac{4}{3}\nu|\tilde{\nabla}.u|^2$ (dot-dashed line). (c) Dissipation rates per unit mass: dE/dt (solid line), expansion-driven damping Q_{exp} (dotted line), visco-resistive dissipation Q_ν (dashed line), and nonlinear loss during cascade Q_{NL} (dot-dashed line, thick when increasing the decay rate and thin when decreasing the decay rate). (d) Temperature compensated by $1/R$ decrease. Distance is normalized by the initial distance $R_0 = 0.2$ au.

comparable as expected, the compressible dissipation decreases rapidly and becomes 1/10 of the total dissipation at the end.

Panel (c) of Figure 2 shows the total energy (Equation (43)) decay rate $|de/dt|$ (solid line) and its components: the expansion decay rate Q_{exp} (dotted line), the turbulent decay rate Q_ν (dashed line), and the residual term Q_{NL} (dot-dashed line). One can distinguish two phases: (a) a short initial transient, during which the turbulent dissipation dominates the expansion decay, in agreement with the small value of the expansion parameter $\epsilon = 0.2$ and a very large residual term comparable to the turbulent dissipation, $Q_{exp} < Q_\nu \simeq Q_{NL}$; and (b) the rest of the evolution, during which the turbulent decay is smaller than the expansion decay, and the residual decay is the smallest, $Q_{NL} < Q_\nu < Q_{exp}$. These two points will be clarified in the discussion. We also remark that the sign of Q_{NL} varies: it is an energy loss (thus increasing $|de/dt|$), denoted by a thick line, but during the beginning phase ($1 \leqslant R/R_0 \leqslant 2$; thin line), it is an energy gain, thus decreasing $|de/dt|$.

Finally, panel (d) gives the resulting temperature curve, compensated by a $1/R$ law. One sees that a power-law regime appears for $R \geqslant 0.5$ au, with an index between 4/3 and 1. The turbulent energy reservoir is clearly used in two phases: (i) an early phase with rapid and strong dissipation that almost stops the plasma cooling and (ii) a long-lasting phase with reduced dissipation that only mildly delays the cooling of the plasma.

3.2. Varying Spectral Extent

Is the set of initial conditions made for run A the most efficient in terms of resulting temperature curve, or can we achieve a resulting curve closer to the observed $1/R$ decrease?
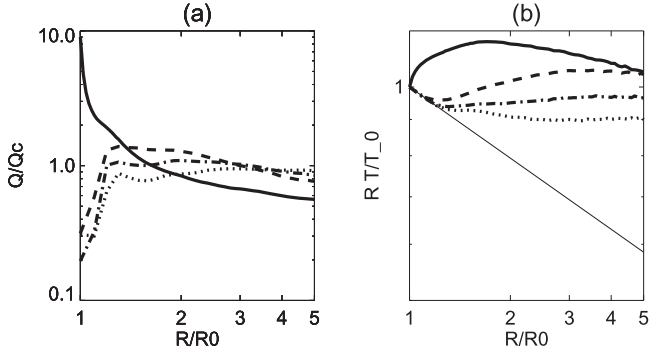
Figure 3. Heating ratio Q_ν/Q_c and temperature profiles, all with $M = 1$, $\epsilon = 0.2$ but varying small-scale initial excitation. Runs A (solid line), B (dotted line), C (dashed line), and E (dot-dashed line). (a) Heating ratio Q_ν/Q_c vs. heliospheric distance R. (b) Average temperature (normalized by its initial value) compensated by R_0/R. Distance is normalized by the initial distance $R_0 = 0.2$ au. The thin solid line in panel (b) corresponds to $T/T_0 = (R/R_0)^{-4/3}$.

As we will see later in the discussion, an important characteristic of run A is the exaggerated importance of small scales, compared to the one found in the quasi-stationary turbulent state. This is at the origin of the excessive heating occurring in the early phase of the run. To reduce the energy of small scales, we now change one or two of the following parameters: (i) the initial spectral slope m and (ii) the initial power-law extent, as measured by $k_{\max}$.

In Figure 3, we compare runs A (solid line), B (dotted line), C (dashed line), and E (dot-dashed line) with the following values of m and $k_{\max}$: $m = 5/3$ and $k_{\max} = 64$ for run A, $m = 3$ and $k_{\max} = 64$ for run B, $m = 5/3$ and $k_{\max} = 4$ for run C, and $m = 2.2$ and $k_{\max} = 4$ for run E. Panel (a) shows the critical heating ratio Q_ν/Q_c that in principle reveals how close we are from critical heating; panel (b) shows the temperature curve compensated for a $1/R$ decrease.

Run A shows an initial large overheating phase with $Q_\nu/Q_c \simeq 10$, followed by insufficient heating $Q_\nu/Q_c < 1$ for $R > 0.3$ au (panel (a), solid line). This explains the different phases of temperature evolution considered earlier: a large part of the turbulent energy is lost during the first phase; so, in the second phase, the remaining turbulent energy is too small to substantially heat the plasma, leading to a temperature decrease between adiabatic and $1/R$ (panel (b), solid line).

Due to the reduced importance of small scales, runs B, C, and E show a different behavior. Initially, for $R \lesssim 1.2$, all of them show comparable critical heating ratios (panel (a)), too small to lead to observable heating. This phase corresponds to a quasi-adiabatic decrease of temperature (panel (b)). This is followed by a quasi-stationary regime ($R \gtrsim 1.2$) in which the heating is close to critical and leads to a common temperature decrease, with all three temperature curves showing a quasi-plateau, thus close to a $1/R$ decrease (panel (b)).

Decreasing the importance of small scales in the initial spectrum thus succeeds in suppressing the too-large energy loss of the first phase. Note that run E shows the profile closest to $1/R$ during the whole nonadiabatic phase. In the following runs, we thus fix the spectral parameters as in run E: spectral slope 2.2 and a short spectral extent with $k_{\max} = 4$.

3.3. Mach Number, ϵ, and M^2/ϵ

Decreasing the initial Mach number intuitively decreases the turbulent energy reservoir compared to the internal energy, so it
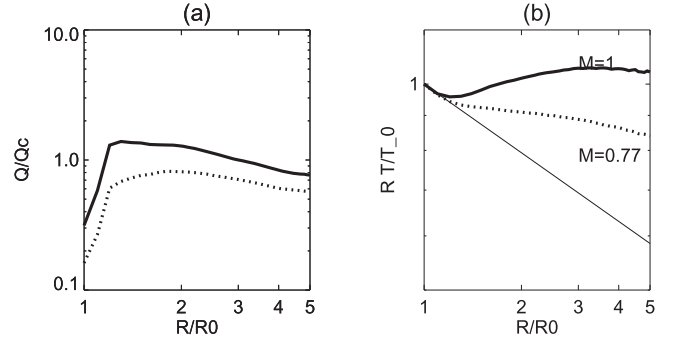
Figure 4. Heating ratio Q_ν/Q_c and temperature profiles, with same $\epsilon = 0.2$ but varying initial Mach number, for runs C ($M = 1$; solid line) and D ($M = 0.77$; dotted lines). Same caption as Figure 3.
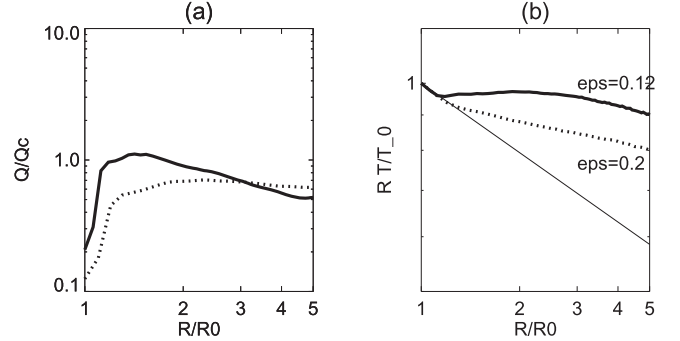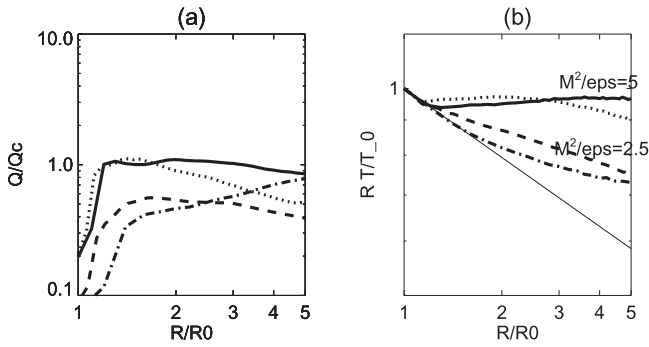

Figure 5. Heating ratio Q_ν/Q_c and temperature profiles, with same $M = 0.77$ but varying expansion parameter, for runs F ($\epsilon = 0.12$; solid line) and K ($\epsilon = 0.2$; dotted line). Same caption as Figure 3.

should also decrease the heating ratio Q_ν/Q_c. In order to check this conjecture, we compare two runs, C and D, both with $k_{\max} = 4$, $\epsilon = 0.2$, and, respectively, $M = 1$ and $M = 0.77$. Figure 4(a) shows that our conjecture for the heating ratio is correct. As a consequence, the average radial slope of the temperature profile changes substantially (Figure 4(b)). Note, however, that the temperature curve shows a break and decreases at a faster rate in the end.

The expansion parameter ϵ measures the expansion rate normalized by the nonlinear shearing rate. Intuitively again, a low expansion parameter should favor heating to the detriment of cooling. In order to check this second conjecture, we compare two values of the expansion parameter, $\epsilon = 0.12$ (run F) and $\epsilon = 0.2$ (run K), with $M = 0.77$ in both cases. The result is as expected (Figure 5); i.e., the heating is larger for the run with lower ϵ during the first part of the transport for $R < 0.6$ au ($R/R_0 < 3$). However, the reverse is true for the second half of the travel. This happens because, for smaller values of ϵ (run F, solid line), the same travel distance corresponds to a larger number of nonlinear times (i.e., larger "age"; see Grappin et al. 1991), which may easily result in a too-fast decrease of the energy reservoir and thus of the heating rate.

Last, we test the parameter M^2/ϵ as a possible control parameter for the heating and temperature profile (see Section 2.3). We choose two pairs of runs: E and F have the largest parameter value, $M^2/\epsilon = 5$, and G and H have the lowest one, $M^2/\epsilon \simeq 2.5$ (see Table 1).

Figure 6(a) shows that the ordering of critical heating by M^2/ϵ is approximately verified for $R < 0.5$ au but not at larger distances. Nevertheless, the temperature curves (Figure 6(b))

Figure 6. Heating ratio Q_ν/Q_c and temperature profiles, with varying M^2/ϵ, for runs E (solid line), F (dotted line), G (dashed line), and H (dot-dashed line). Same caption as Figure 3.

Figure 7. Heating ratio Q_ν/Q_c and temperature profiles, with $M = 0.77$, $\epsilon = 0.2$, and varying β, for runs M (solid line; $\beta = 2.75$), N (dotted line; $\beta = 1.48$), and K (dashed line; $\beta = 0.49$). Same caption as Figure 3.

appear to be gathered in two groups according to the parameter value.

3.4. Varying the Plasma β and Angle θ_{VB}

Due to variations of the initial temperature, with the mean initial magnetic field remaining constant, the β of the different runs considered up to now (runs A to K) has been varied in the interval $0.3 \leqslant \beta \leqslant 0.8$ (Table 1). Since, in the slow solar wind, the β of the plasma can be larger than unity, we now consider runs with larger values, $\beta = 2.75, 1.48$ (runs M and N), and compare with run K with $\beta = 0.49$. The Mach number is 0.77 in the three runs. The overall effect of the β variation appears to be small (Figure 7), with, however, a slight advantage (stronger heating) to the two runs with larger β (runs M and N; solid and dotted lines with quasi-superposed curves).

A last parameter is of interest: it is well known that, although the angle θ_{VB} between the magnetic field and the radial direction is, on average, $45°$ at 1 au (which corresponds to $\theta = 11°$ at 0.2 au), its distribution actually varies widely around the average. To test the effect of small-angle variation, we considered doubling the initial angle θ_{VB}^0. We found that when passing from $\theta_{VB}^0 = 11°$ to $\theta_{VB}^0 = 20°$, the critical heating ratio, as well as the temperature profile, shows no variation at all (not shown).

4. Discussion

4.1. Summary

Our numerical results support the possibility that MHD turbulence can drive a proton temperature profile that is decreasing significantly more slowly than the adiabatic prediction in the distance range $0.2 < R < 1$ au. We started with a spectrum initially having a 2D configuration, corresponding in principle to the slow wind regime as observed by Dasso et al. (2005). This led, with an rms Mach number close to unity and expansion parameter $\epsilon = 0.2$, to a temperature profile significantly steeper than observed; however, when considering a strong reduction of the initial spectral inertial range, we obtained a temperature profile close in average to a $1/R$ law, thus not far from the average $1/R^{0.9}$ profile measured by Totten et al. (1995).

We found that the parameters regulating the heating rate are the rms Mach number and the expansion parameter ϵ, combined as M^2/ϵ, while other parameters, such as plasma β and angle θ_{VB} between the mean field and the radial (for small initial values) have a minor effect.
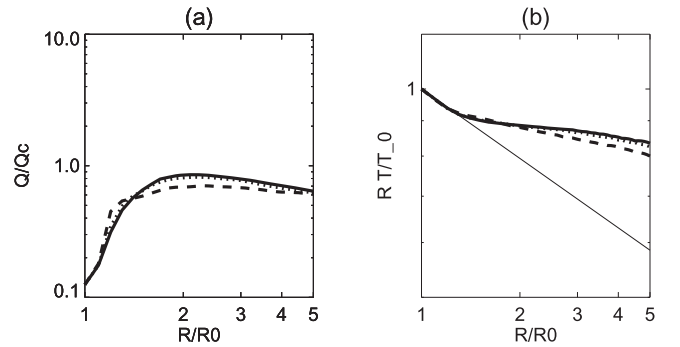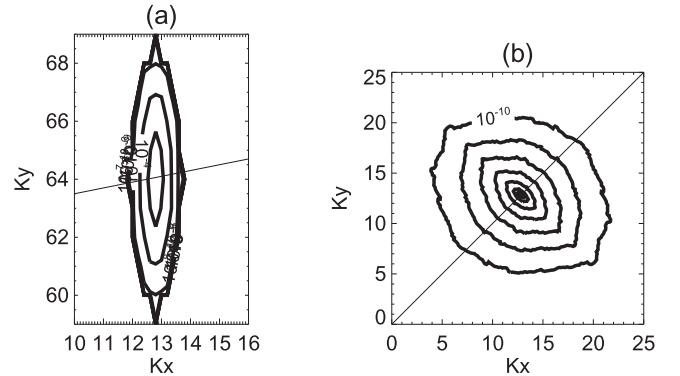

Figure 8. Run E: rotation of the energy spectrum (kinetic + magnetic) with the mean magnetic field. The angular energy spectrum $E(k_x, k_y)$ is in the plane $k_z = 0$. (a) At $R = 0.2$ au. (b) At $R = 1$ au. The mean magnetic field direction is represented by a straight line in each panel.

4.2. Spectral Properties versus Mach Number

To understand the necessity of reducing the initial small-scale energy content, we examine here the spectral evolution.

We first examine the spectral anisotropy. Figure 8 shows the case of run E; it is representative of the other runs that all show comparable evolutions. The 2D spectra shown are cuts though the plane $k_z = 0$ of the 3D spectrum for total energy $u^2 + \delta B^2/\rho$. As explained in Section 2, the initial energy isocontours (panel (a); $R = 0.2$ au) are quasi-perpendicular to the mean field direction (straight line), which is close to the radial direction. At 1 au, however (panel (b)), the mean magnetic field has an angle of $\pi/4$ with the radial, and the main symmetry axis of the isocontours is now quasi-perpendicular to this mean field. In other words, the cascade is not only initially perpendicular to the mean field, it remains so during transport, following the rotation of the mean field. This corresponds nicely to the so-called 2D spectrum dominant in the slow wind (Dasso et al. 2005), which was first found numerically in Verdini & Grappin (2016) to be one of the two robust attractors in the wind.

We now consider the 1D reduced total energy spectra at 0.2 and 1 au for runs A, B, C, and E, shown in Figure 9. The initial spectra have dotted lines, and the final ones have solid lines (1 au). The final spectra depend on either radial (thick solid line) or perpendicular (thin solid line) wavevectors. The wavenumber is normalized by the Kolmogorov dissipation wavenumber $k_d = (Q_\nu/\mu^3)^{1/4}$, where the dissipation rate Q_ν is defined in Equation (27). Each final spectrum is then obtained
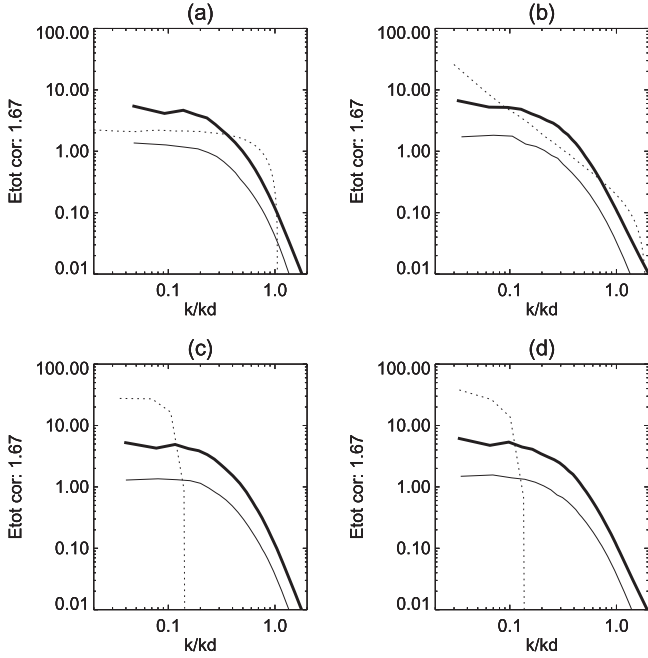
Figure 9. Runs A, B, C, and E: evolution of the 1D energy spectrum (kinetic + magnetic), compensated by the Kolmogorov scaling $k^{-5/3}$. Abscissa: wavenumber normalized by the Kolmogorov wavenumber $k_d = (Q_\nu/\mu^3)^{1/4}$. Dotted line: $R = R_0 = 0.2$ au. Solid lines: $R = 1$ au. Thick solid line: radial 1D spectrum. Thin solid line: 1D spectrum perpendicular to radial ($\hat{z}$ direction).

by averaging the spectra so normalized in the distance interval $0.6 \leqslant R \leqslant 1$.

The four final spectra are all comparable (either along the radial or transverse direction), showing a very reduced spectral extent of about half a decade with a slope $m \gtrsim 5/3$.

The origin of the small extent of the inertial range in the final spectra actually lies in the high Mach number ($M = 1$) adopted in these runs. A high Mach number leads to large intermittent variations of density associated with shocks, thus requiring large viscosities to prevent the occurrence of unresolved gradients in high-density regions. As a matter of comparison, when dealing with run Z ($M = 0.33$), we could use a viscosity 10 times smaller than that used for runs with $M = 1$ (see Table 1). Due to its much lower viscosity, run Z follows a $k^{-5/3}$ scaling on more than one decade, thus significantly larger than that for run A (Figure 10).

The short spectral extent seen previously for runs with $M = 1$ thus results from the necessity to increase the viscosity with such large Mach numbers to prevent a catastrophic (unphysical) evolution of the run at a given numerical resolution. This also explains why it is necessary to start with a small spectral extent: otherwise, during a transient phase, one obtains excessive heating produced by the artificial initial excess of energy at visco-resistive scales (see the evolution of Q_ν/Q_c for run A in Figure 3(a)).

4.3. Dissipation Rate and Kolmogorov Rate

The parameter M^2/ϵ (Equation (42)), derived in Section 2.3, has been used to specify conditions allowing us to approach critical heating. In particular, in runs B, C, and E, the value $M^2/\epsilon = 5$ (not too far from the nominal value of 4.4 derived in Equation (42)) allowed us to obtain temperature profiles with a power law close to $1/R$.
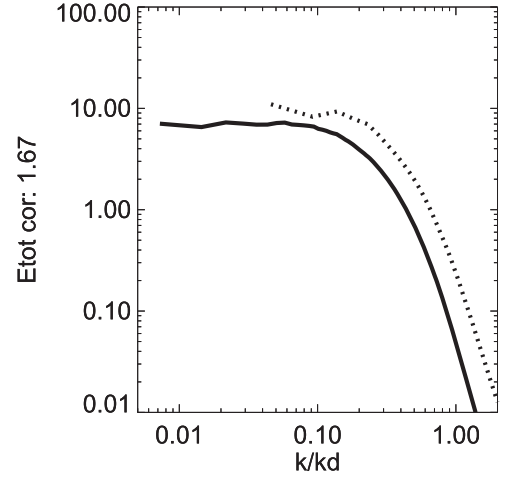
Figure 10. Runs Z (solid line) with $M = 0.3$ and A (dotted line) with $M = 1$. The total 1D energy spectrum is averaged during the last phase of transport, compensated by the $k^{-5/3}$ scaling. Abscissa: radial wavenumber normalized by the Kolmogorov wavenumber.
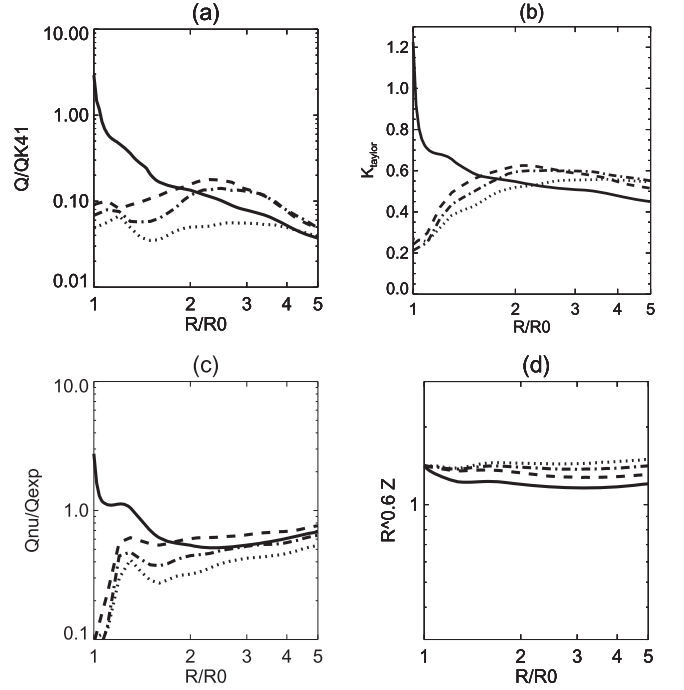
Figure 11. Checking the Vasquez law and consequences. (a) Ratio Q_ν/Q_{K41} between visco-resistive dissipation and Kolmogorov's energy cascade rate (Equation (36)). (b) Radial Taylor wavenumber. (c) Ratio Q_ν/Q_{exp} between visco-resistive dissipation and expansion decay rate. (d) Turbulent rms amplitude $Z = (u^2 + \delta B^2/\overline{\rho})^{1/2}$ evolution compensated by $1/R^{0.6}$. Shown are runs A (solid line), B (dotted line), C (dashed line), and E (dot-dashed line).

The argument used in Section 2.3 leading to this prescription relies on the assumption that the ratio $R_V = Q_\nu/Q_{K41}$ is $\simeq 0.1$. This very low value of R_V (corresponding to an effective very high Kolmogorov constant) has been found to hold in cold winds by Vasquez et al. (2007). It would be satisfying to check whether or not the runs studied in this paper show the same low value of R_V.

Figure 11(a) gives R_V versus distance in runs A, B, C, and E. The curve varies wildly for run A, with R_V passing from larger than 1 to lower than 0.1, while runs B, C, and E all show a ratio clustering around the value 0.1 on the whole distance range.

Panel (b) shows the evolution of the Taylor wavenumber (Equation (37)) for the four runs, summarizing the spectral width evolution for the different runs. By comparing panels (a) and (b), one sees again that the initial oversized spectral width of run A leads to an anomalously large value of R_V. In contrast, runs B, C, and E, which have a spectral width adapted to their viscosity, show R_V values clustering around 0.1.

The fact that in our simulations B, C, and E leading to a critical heating, we find a value for Q_ν/Q_{K41} close to that observed indicates that our numerical setup, in spite of the previous remarks on the limited spectral range, leads to turbulent properties close to those of the actual solar wind turbulence.

This small value of R_V means that the characteristic turbulent decay time is about 10 times longer than the plain nonlinear time $t_{NL} = 1/ku$. This allows us to interpret the relative importance in our runs of the expansion decay rate and turbulent decay rate. Indeed, with an expansion parameter $\epsilon = 0.2$, as in runs A, B, C, and E, one expects a priori an expansion decay rate Q_{exp} smaller than the turbulent dissipation rate, since ϵ is the expansion rate normalized by the inverse of the turnover time at large scales (Equation (13)). However, due to R_V being 0.1, the effective turbulent decay timescale is 10 times longer than the nonlinear turnover time. The effective expansion decay rate is thus finally not smaller, but rather larger than the turbulent dissipation rate, in spite of $\epsilon = 0.2$. This is true in the whole distance range [0.2, 1] au for runs B, C, and E, and also for run A, except during the early transient where R_V is close to unity.

A corollary to the overall dominance of expansion damping in runs A, B, C, and E should be that the turbulent fluctuation amplitude decays close to the WKB prediction, which is, for Alfvén waves,

$$Z = (u^2 + \delta B^2/\overline{\rho})^{1/2} \simeq 1/R^{1/2}. \tag{47}$$

This is indeed the case: Figure 11(d) shows that the turbulent amplitude in runs A, B, C, and E decays as $Z \simeq 1/R^{0.6}$, thus close to the WKB prediction.

4.4. Loss of Energy Conservation during Cascade

The deviation from turbulent energy conservation during cascade has been measured by the residual term Q_{NL}, defined as the difference between the total turbulent energy decay and the sum of turbulent dissipation Q_ν and linear expansion decay Q_{exp} (Equation (46), run A, Figure 2(c)). Other runs show that with a fixed Mach number, the residual term Q_{NL} is proportional to the expansion parameter ϵ. In order to eliminate the contribution of compressibility and so to determine without ambiguity the contribution of expansion alone, we consider the deviation of total energy conservation instead of just turbulent energy. We denote the new residual term by $Q_{NL'}$:

$$d/dt(e + \langle \tilde{\rho}T \rangle/(\gamma - 1)) = -Q_{exp} - 2\gamma\langle \tilde{\rho}T \rangle \epsilon/a - Q_{NL'}. \tag{48}$$

Figure 12 shows the total (turbulent + internal) energy time derivative and the associated residual term $Q_{NL'}$ for run A. The residual dissipation is limited to 1% or 2% of the total variation. This is substantially smaller than Q_{NL} (see Figure 11(c)). It shows that compressible exchanges between turbulent and internal energy are the dominant contribution to
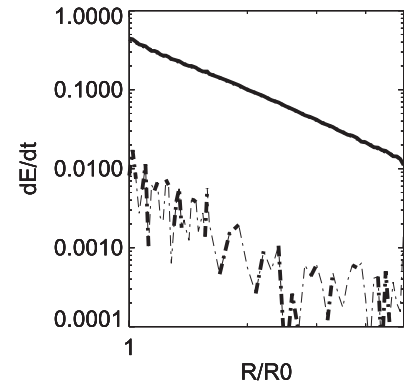
Figure 12. Run A: deviation from total (turbulent + internal) energy conservation during cascade. Solid line: time derivative of total energy (turbulent + internal, Equation (48)). Dot-dashed line (thick when increasing the decay rate, thin when decreasing the decay rate): residual term $Q_{NL'}$ measuring the deviation from total energy conservation during the cascade apart from linear effects.

the deviation of turbulent energy conservation during the cascade, especially during the beginning of the evolution. The same remarks can be made for the other runs in Table 1. However, in run H, with a larger expansion parameter ($\epsilon = 0.4$), we find that compression and expansion contribute more equally (not shown).

4.5. Conclusion

In conclusion, using complete nonlinear couplings of MHD equations, we have shown that radial temperature profiles as $1/R$ simply result from the combination of adiabatic decrease and turbulent dissipation. This has been done starting at 0.2 au with an rms Mach number 1 and an expansion parameter $\epsilon = 0.2$. With these parameters, the decrease of rms turbulent amplitude is not much faster than the Alfvén WKB prediction, actually as $1/R^{0.6}$. This demonstration has been done by starting with a spectral anisotropy characteristic of slow winds, namely mainly perpendicular to the mean magnetic field. This included showing that the Q_ν/Q_{K41} ratio is close to 0.1 in our simulations, as in the solar wind. Finally, we measured the deviation from the conservation of turbulent energy during the cascade (residual energy loss Q_{NL}). We found that expansion was a minor cause of deviation, the main cause being compressible exchanges between turbulent and internal energy.

Future work includes (i) providing a clearer signature (i.e., with larger Reynolds) of the 5/3 power-law index characteristic of slow winds by lowering the Mach number and the expansion parameter and (ii) considering the case of fast winds, which, despite having a different spectral anisotropy, produce a similar radial dependence of the temperature.

ORCID iDs

Victor Montagud-Camps ⓘ https://orcid.org/0000-0002-7848-9200
Roland Grappin ⓘ https://orcid.org/0000-0001-7847-3586
Andrea Verdini ⓘ https://orcid.org/0000-0003-4380-4837

References

Breech, B., Matthaeus, W. H., Cranmer, S., Kasper, J. C., & Oughton, S. 2009, JGRA, 114, A09103

Carbone, V., Marino, R., Sorriso-Valvo, L., Noullez, A., & Bruno, R. 2009, PhRvL, 103, 61102

Coburn, J. T., Smith, C. W., Vasquez, B. J., Stawarz, J. E., & Forman, M. 2012, ApJ, 754, 93

Dasso, S., Milano, L. J., Matthaeus, W. H., & Smith, C. W. 2005, ApJL, 635, L181

Dong, Y., Verdini, A., & Grappin, R. 2014, ApJ, 793, 118

Grappin, R., & Velli, M. 1996, JGR, 101, 425

Grappin, R., Velli, M., & Mangeney, A. 1991, AnGeo, 9, 416

Grappin, R., Velli, M., & Mangeney, A. 1993, PhRvL, 70, 2190

Hellinger, P., Travnicek, P., Štverák, Š., Matteini, L., & Velli, M. 2013, JGRA, 118, 1351

Marino, R., Sorriso-Valvo, L., Carbone, V., et al. 2008, ApJL, 677, L71

Matthaeus, W. H., & Velli, M. 2011, SSRv, 160, 145

Politano, H., & Pouquet, A. G. 1998, PhRvE, 57, 21

Scudder, J. D. 2015, ApJ, 809, 126

Smith, C. W., Matthaeus, W. H., Zank, G. P., et al. 2001, JGR, 106, 8253

Stawarz, J. E., Smith, C. W., Vasquez, B. J., Forman, M., & MacBride, B. T. 2009, ApJ, 697, 1119

Totten, T. L., Freeman, J. W., & Arya, S. 1995, JGR, 100, 13

Tu, C.-Y. 1988, JGR, 93, 7

Tu, C.-Y., & Marsch, E. 1997, SoPh, 171, 363

Vasquez, B. J., Smith, C. W., Hamilton, K., MacBride, B. T., & Leamon, R. J. 2007, JGR, 112, A07101

Verdini, A., & Grappin, R. 2016, ApJ, 831, 179

Verdini, A., Grappin, R., Hellinger, P., Landi, S., & Müller, W. C. 2015, ApJ, 804, 119